Distribution of structural domains in MnAs layers grown on GaAs substrates

Y. Takagaki,[a] J. Lähnemann, B. Jenichen, J. Herfort, C. Herrmann, and U. Jahn
Paul-Drude-Institut für Festkörperelektronik, Hausvogteiplatz 5-7, 10117 Berlin, Germany

Electron backscatter diffraction is utilized to determine the distribution of coexisting structural domains in MnAs layers prepared on GaAs substrates. In a layer grown on a GaAs(111)B substrate using solid phase epitaxy, the structural domains roughly correspond to the morphological features of the surface. The domains are, in contrast, considerably larger in size than the surface roughness when the substrate is GaAs(113)A. We examine the role of the freedom in in-plane crystalline alignment for causing such a difference using a numerical model. In a layer grown at an extraordinary high temperature (600 °C) on a GaAs(111)B substrate, (0001) and $(1\bar{1}0l)$ orientations are interwoven. While the (0001) component is present mainly as thin flat films, a mixture of all the components forms thick elongated islands in the surrounding of the films. Consequences of such an inhomogeneity on the magnetic and electrical properties of the layer are discussed. © 2010 American Institute of Physics. [doi:10.1063/1.3520654]

I. INTRODUCTION

In the growth of MnAs layers on GaAs substrates, the lattice-mismatch strain relaxes almost completely when the layer thickness is merely a few nanometer.[1,2] The small critical thickness for coherent growth manifests remarkable importance of the strain energy in comparison to the bonding energy at the MnAs–GaAs heterointerface. The overwhelmingness of the strain energy was utilized to realize unconventional epitaxial orientations by means of solid phase epitaxy (SPE), in which least lattice-mismatched orientations were favored despite generation of dangling bonds.[3–5]

MnAs is a ferromagnetic metal having the Curie temperature above room temperature ($T_C \approx 40$ °C). The magnetocrystalline anisotropy in MnAs is notably strong with the magnetic hard axis being oriented in the direction of the *c* axis. (The crystal structure of MnAs is hexagonal.) Conventionally, the epitaxial orientation of MnAs layers has been varied by selecting the substrate orientation and growth conditions.[6] The extended controllability of the epitaxial orientation relationship accomplished by SPE is beneficial in designing magnetic devices and for spintronics applications.

In the MnAs layers prepared on GaAs(111)B and GaAs(113)A surfaces by SPE, structural domains inevitably exist as there are, respectively, three and two equivalent in-plane directions of the substrates to which the MnAs crystal is aligned.[3,5] The surface morphology, as a consequence, develops characteristic features as grains having sizes of a few hundred nanometer are clearly visible.

In this paper, we investigate the correspondence between the surface roughness features and the structural domains using electron backscatter diffraction (EBSD). The mapping of the distribution of the structural domains reveals that the relationship between the domain configuration and the surface morphology are not the same for the MnAs layers on GaAs(111)B and GaAs(113)A. We explain the observation in terms of the difference in the degree of freedom in the in-plane crystalline alignment and the faceting of the surface. In addition, we apply the EBSD analysis for a MnAs layer grown at an unconventionally high temperature, in which a variety of crystal orientations make up a markedly inhomogeneous surface landscape. We interpret the magnetic and electrical properties of the layer based on the thus identified distribution of structural domains.

II. LAYER GROWTH

The MnAs layers were grown in a molecular beam epitaxy (MBE) chamber. In the procedure of SPE,[3] an amorphous MnAs layer with a thickness of 2 nm was deposited at a substrate temperature of 200 °C. In the heterostructures that we refer to as samples 1 and 2, the GaAs substrates were (111)B- and (113)A-oriented, respectively. The amorphous layers crystallized during heating of the substrates to the growth temperatures for ordinary MBE growth of MnAs, which are 270 °C and 250 °C for GaAs(111)B and GaAs(113)A substrates, respectively. We point out that amorphous MnAs layers can be prepared by lowering the substrate temperature merely 50–70 °C from the optimum growth temperature. This makes SPE a convenient tool to vary the epitaxial orientation.

Employing the crystallized layers as a template, the layer thickness was increased by a conventional epitaxial growth at the raised substrate temperatures. The reflection high energy electron diffraction (RHEED) pattern did not change during the latter growth, indicating that the layers grew maintaining the crystal orientations of the templates. The RHEED intensity was nearly unchanged, suggesting that the surface morphology was also preserved. The As_4/Mn beam-equivalent pressure (BEP) ratio was 420 for the deposition of the amorphous layer and 28 for the conventional growth for sample 1. For sample 2, the BEP ratio was 100 throughout the growth procedure. The MnAs layers are 50 nm and 150 nm thick for samples 1 and 2, respectively.

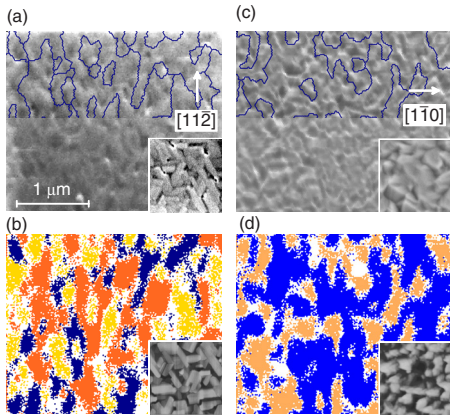[a]Electronic mail: takagaki@pdi-berlin.de.

FIG. 1. (Color online) Surface images [(a) and (c)] and distribution of structural domains [(b) and (d)] obtained by EBSD analysis. The MnAs layers were prepared using SPE on GaAs(111)B, sample 1, and GaAs(113)A, sample 2, substrates for the left- and right-hand-side columns, respectively. The scan area is 3×2.5 μm^2 large. The $[1\bar{1}0]$ direction of the substrates is set in the horizontal direction. Major domain boundaries are depicted in the top part of (a) and (c). In (b), the c axis of the $(1\bar{1}00)$-plane is tilted from the vertical direction by $-60°$, $0°$, and $60°$ in the blue (dark gray), orange (medium gray), and yellow (light gray) areas, respectively. In (d), the c axis of the $(21\bar{3}1)$-plane is tilted by $\pm42.7°$ away from the vertical direction for the two colored areas. Identification of Kikuchi pattern failed in the white area. The insets in (a) and (c) show SEM images viewed actually in the direction of the surface normal. The insets in (b) and (d) show AFM images. The scale of the images in the main panels and insets is identical.

For the other sample, sample 3, a MnAs layer was grown on a GaAs(111)B substrate at a substrate temperature of 600 °C. The growth was carried out by means of conventional MBE, i.e., the SPE procedure was not used. The BEP ratio was 350 with a growth rate of 20 nm/h. The nominal layer thickness is 50 nm. With such an extremely high growth temperature, MnAs layers were observed to develop elongated islands, as we describe below. It is noteworthy that 600 °C was also the growth temperature for the GaAs buffer layer. Thus, understanding of the growth dynamics at the high substrate temperature and of the structural properties of the grown layers may enable us to fabricate buried MnAs layers inserted between GaAs layers.[7]

III. DISTRIBUTION OF DOMAINS

A. Layers prepared using SPE

In Figs. 1(a) and 1(c), we show scanning electron microscope (SEM) images of the surface of, respectively, samples 1 and 2 obtained in the EBSD analysis. Because of the high stage tilt (70°) needed in the EBSD technique, the surface morphology is considerably smeared and distorted. We have, therefore, included in the insets SEM images actually viewed in the direction of the surface normal. We have also added atomic force microscope (AFM) images in the insets of Figs. 1(b) and 1(d). (The SEM and AFM images provided in the insets do not correspond to each other.) The surfaces are not smooth in these layers because of structural domains. The root-mean-square amplitude of the surface roughness estimated using AFM was 2.1 nm and 4.1 nm for samples 1 and 2, respectively.

The MnAs layer on GaAs(111)B is $(1\bar{1}00)$-oriented with the c axis being aligned in the $\langle11\bar{2}\rangle$ directions of the substrate.[3] The c axis can, therefore, be oriented along any of three equivalent in-plane directions, giving rise to the sixfold-symmetric texture composed of elongated grains, see the inset of Fig. 1(b). Here, the $[1\bar{1}0]$ direction of the substrate is aligned horizontally in the panel, i.e., the c axis of MnAs is perpendicular to the elongation of the grains.

In the MnAs layer on GaAs(113)A, the epitaxial orientation is $(21\bar{3}1)$. As investigated in Ref. 5, the direction of the c axis projected to the surface plane is tilted from the $[33\bar{2}]$ direction of the substrate toward the $[\bar{1}10]$ direction by $\pm42.7°$. From the viewpoint of the lattice period, there are four equivalent surface directions to which the c axis of MnAs can be aligned. However, the in-plane polarization of the GaAs(113) surface in the $[33\bar{2}]$ direction reduces the number of structural domain types realized in the layer to two.[5] In spite of the existence of such an order, the roughness shown in the inset of Fig. 1(d) has no obvious symmetry and bears an appearance of being random. The shape of individual grains may thus be suggested to be nearly isotropic for the layer on GaAs(113)A while it is anisotropic for the layer on GaAs(111)B.

The distribution of the structural domains revealed by EBSD is shown in Figs. 1(b) and 1(d) for the regions shown in Figs. 1(a) and 1(c), respectively. The EBSD measurements and analysis were carried out using the EDAX OIM software. The acceleration voltage was 15 keV, for which the fundamental spatial resolution is about 20 nm. The solid curves in Figs. 1(a) and 1(c) depict the major domain boundaries extracted from the top part of Figs. 1(b) and 1(d). As one would expect from the characteristic that the grain texture in sample 1 reflects the rotation symmetry of the substrate surface, small structural domains almost exactly correspond to the elongated islands. In comparison, the domain size in sample 2 is considerably larger than the length scale of the roughness, i.e., even the surface of small domains is not featureless.

The typical grain size in the AFM images is similar between samples 1 and 2 ($\sim$50 nm). However, the length scale of the roughness in the SEM images is smaller in sample 2 than in sample 1. The surface of an individual structural domain in sample 2 contains several facets, instead of a single $(1\bar{1}00)$ plane in sample 1, as the $(21\bar{3}1)$ surface is almost certainly unstable. The faceting makes the different length scales between the morphology and the domain distribution in sample 2 even more pronounced.

The domain size can be, in general, larger than the grain size as crystal orientations in adjacent grains may be identical by chance. The fewer degrees of freedom in the in-plane crystalline alignment in sample 2 in comparison to sample 1 are thus anticipated to be responsible for the larger domain size in Fig. 1(d) than in Fig. 1(b). We have, therefore, examined the influence of the coincidental alignment on the domain size using a simple theoretical model. As the actual shape of the grains in samples 1 and 2 is not known, we assume square and hexagonal lattices, in which square and
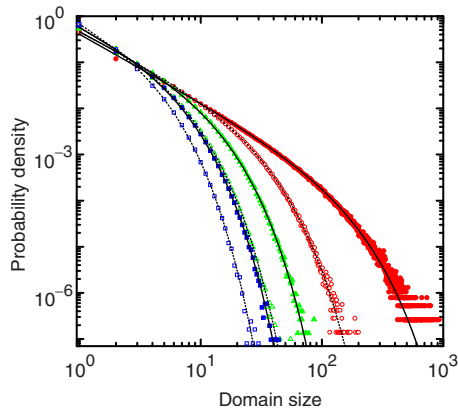
FIG. 2. (Color online) Distribution of domain size, i.e., the probability density $p(s)$ vs domain size s, obtained by numerical simulations. The filled and open symbols correspond to, respectively, square and hexagonal lattices consisting of 10^6 cells. Periodic boundary conditions were assumed. The degree of freedom f of the "crystal orientation" in each cell is 2, 3, and 4 for the circles (red), triangles (green), and squares (blue), respectively. The lines show fits to a form given in Eq. (1). The values of the fit parameters are plotted in Fig. 3.

FIG. 3. (Color online) Values of parameters γ, (a), and c, (b), used in the fits shown in Fig. 2. A c-vs-ln f graph is shown in the inset of (b). The average domain size $\langle s \rangle$ and a ratio $A/\langle s \rangle$ are plotted in (c). The filled and open symbols correspond to the square and hexagonal lattices, respectively. The solid lines show a linear dependence with the f-intercept 1.5 and 2.

triangular cells represent the grains. The two types of lattices were chosen in order to correspond to fourfold and threefold symmetry substrates. We assign the "crystal orientation" within a cell randomly according to the degree of freedom f. That is, a cell is designated to be in one state among f possibilities with uniform probabilities. We have then calculated the size of all the domains in the lattices, which is the number of cells that constitute the domains.

As plotted in Fig. 2, the distribution of the domain size s obeys a power law with an exponential cut-off[8–10]

$$p(s) = As^{-\gamma}e^{-cs}. \tag{1}$$

By fitting the probability density $p(s)$ given by Eq. (1) to the numerical data, as shown by the curves in Fig. 2, we determined parameters A, γ, and c, as summarized in Figs. 3(a) and 3(b). The power-law exponent γ is nearly identical (≈ 1.2) for both the square and hexagonal lattices and $f > 2$ (with a slight tendency of smaller γ for larger f).[9] For $f = 2$, γ is somewhat larger. Obviously, large domains become scarce with increasing f. Such a change is implemented in the distribution function by strengthening the exponential cut-off, while the power-law behavior for small domains is left almost unaffected. As shown by the solid lines in Fig. 3(b), c is unexpectedly found to depend nearly linearly on f with the intercept $f_0 = 2$ and 1.5 for the square and hexagonal lattices, respectively. The square lattice with $f = 2$ is thus suggested to be a critical case, which may be related to the abrupt increase of γ. It may be noteworthy that the ratio $A/\langle s \rangle$, where $\langle s \rangle$ is the average domain size, exhibits the same linear dependence, as plotted in Fig. 3(c). (We examine the domain size distribution in quasi-one-dimensional square lattices in Appendix.)

We show experimental results in Fig. 4. The number of domains that we can handle experimentally in evaluating the statistics is much smaller than that in the numerical simulations. Therefore, instead of $p(s)$, we plot in Fig. 4 the probability $P(s)$ of the domain size being larger than s
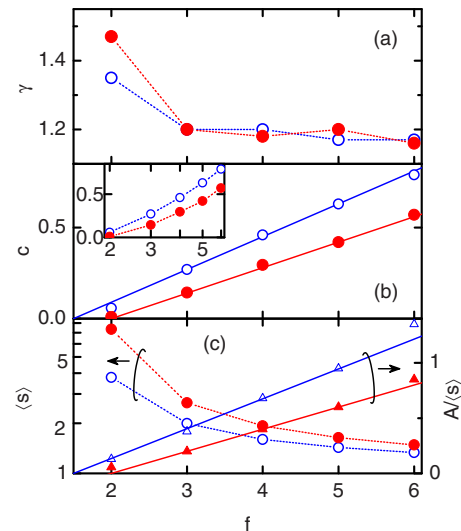
$$P(s) = \int_s^\infty p(\sigma)d\sigma. \tag{2}$$

Note that $P(s) \propto s^{-\gamma+1}$ when $p(s) \propto s^{-\gamma}$. The slope in Fig. 4 is hence in reasonable agreement with the theoretically predicted power-law exponent, as indicated by the dotted line. The large slope for small domain sizes is due to the resolution limit and resultant fit errors in the EBSD measurements, which give rise to artificial ultrasmall domains. (From the transition value in the domain size, the actual spatial resolution is estimated to be about 45 nm, which is reasonable considering the roughness of the surface.) We also point out that the cut-off for large domain sizes may be enhanced in the experimental results due to the finite scan area in the measurements, which was mostly 3×3 μm^2.
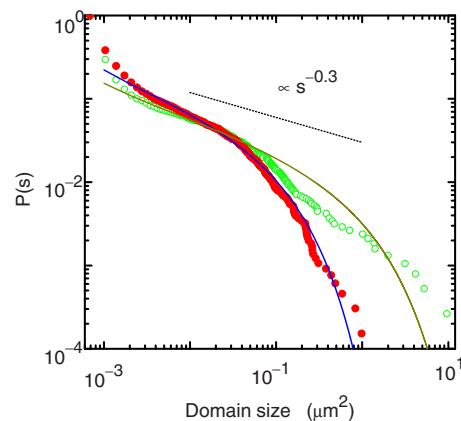

FIG. 4. (Color online) Probability $P(s)$ of the size of structural domains being larger than s. The filled and open circles correspond to samples 1 and 2, respectively. The solid curves are fits assuming a probability density in the form of Eq. (1). The power-law exponent was set to be $\gamma = 1.3$. The cut-off parameter c is 4 and 0.4 μm^{-2} for samples 1 and 2, respectively. The dotted line shows the slope corresponding to $\propto s^{-0.3}$.
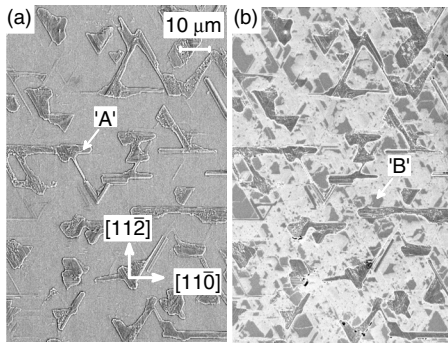
FIG. 5. Scanning electron micrographs of sample 3. Only the thick islands (the type-A islands indicated with "A") are practically seen in (a). The thin films (the type-B islands indicated with "B") are visible in (b), which was taken using the in-lens detector of SEM, in the area surrounding the type-A islands.
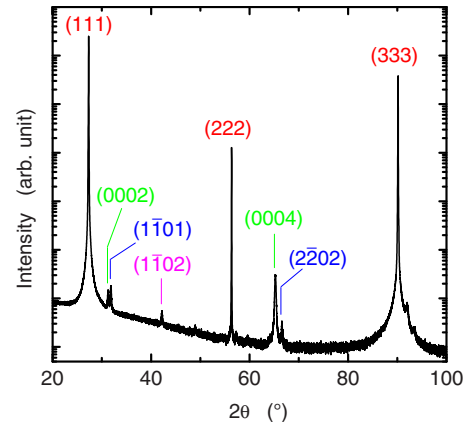

FIG. 6. (Color online) XRD curve (ω-2θ scan) of sample 3. The three- and four-index notations of the reflection peaks refer to GaAs and MnAs, respectively.

The solid curves show fits using distribution functions in the form of Eq. (1). Because of the considerable statistical uncertainties in the experimental data, we assumed $\gamma=1.3$, as anticipated from the simulations, and adjusted c. One finds that the experimental results are satisfactorily described. Clearly, the enlargement of the domain size due to the incidental alignment has to be taken into account in comparing the domain size. The ratio of the cut-off parameters c_f for $f=2$ and 3 in the simulations is $c_3/c_2=14$ and 4.7 for the square and hexagonal lattices, respectively. Experimentally, we find the ratio to be about 10. It is, therefore, conceivable that the difference in the domain size between samples 1 and 2 arose entirely from the degree of freedom $f=3$ and 2 in the respective samples.

B. Layer grown at extremely high temperature

We now turn our attention to sample 3. As apparent in the SEM image shown in Fig. 5(a), the MnAs layer grew highly inhomogeneously at the temperature of 600 °C. The layer developed anisotropic islands, which are elongated along the $\langle 1\bar{1}0\rangle$ directions of the substrate. The anisotropic growth was explored by Xu *et al.*[11] to create nanometer-scale wires on GaAs(001), in which the elongation was in the GaAs[110] direction. Another type of islands is recognized in Fig. 5(b). The elongated islands that are clearly visible in Fig. 5(a), which we refer to as type-A islands, are thick islands that are composed of many grains having various sizes. In the area surrounding the type-A islands, gray patches having hexagonal geometries are seen in Fig. 5(b). These type-B islands are thin films whose surface is remarkably uniform and flat. They are present with various thicknesses, yielding stepped terraces at the domain boundaries.

In Fig. 6, we show an x-ray diffraction (XRD) curve of sample 3. The layer mainly consists of (0001)-, ($1\bar{1}01$)-, and ($1\bar{1}02$)-oriented components. [The expected position of the reflection peaks associated with ($1\bar{1}00$) orientation is very close to the position of the substrate peaks, and so the presence of ($1\bar{1}00$) orientation cannot be evidenced.] While the ($1\bar{1}01$)-reflection peak was larger than the (0002)-reflection peak in amplitude, the relationship was opposite between the

($2\bar{2}02$)- and (0004)-reflection peaks. The reason is unclear at present. Due to this ambiguity, the volume fractions of the components having the various surface orientations could not be estimated from the XRD measurements.

Figures 7(a) and 7(b) show a SEM image and the corresponding distribution of surface orientations determined by the EBSD analysis, respectively. The ($1\bar{1}0l$)-oriented components, including $l=0$, that could not be detected by the XRD measurements as we mentioned above, are found to be present as building blocks of the type-A islands. (0001)-oriented segments are also found as parts of these islands, exhibiting usually flat surfaces within the mosaic pattern of the thick islands. In Fig. 7(c), we show the in-plane alignment of the c axis for the ($1\bar{1}0l$)-oriented components. There
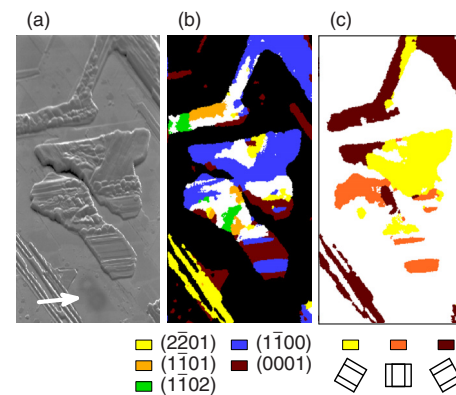

FIG. 7. (Color online) Scanning electron micrograph, (a), and distribution of structural domains [(b) and (c)] obtained by EBSD analysis of sample 3, which is a MnAs layer grown at 600 °C on GaAs(111)B. The scan area is 16×32 μm^2 large. The [$1\bar{1}0$] direction of the substrate is shown by an arrow in (a). In (b), the areas shown by yellow, orange, green, blue, and brown (from light gray to dark gray) correspond to ($2\bar{2}01$)-, ($1\bar{1}01$)-, ($1\bar{1}02$)-, ($1\bar{1}00$)-, and (0001)-orientations, respectively. The tolerance for deviation from the nominal surface orientations was set to be 10°. Only the Kikuchi pattern of the GaAs substrate was detected in the black area. The white area corresponds to other orientations and fit errors. The c axis orientation within the surface plane for the ($1\bar{1}0l$) components is displayed in (c). The inclination of the c axis from the [$11\bar{2}$] direction of the substrate is $-60°$, 0°, and 60° in the yellow (light gray), orange (medium gray), and brown (dark gray) areas, respectively. In the white area, the c-axis orientation is either perpendicular to the plane or unknown.
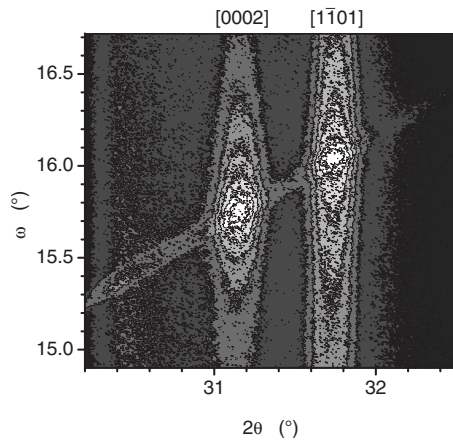
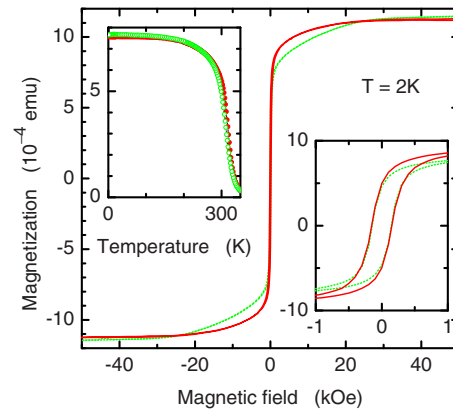FIG. 8. Intensity of XRD in the vicinity of the (0002)- and $(1\bar{1}01)$-reflection peaks in sample 3.

FIG. 9. (Color online) Magnetization curves of sample 3 at a temperature of $T=2$ K. An in-plane external magnetic field was applied in the $[1\bar{1}0]$ and $[11\bar{2}]$ directions of the substrate for the solid and dotted curves, respectively. The right inset shows the hysteresis loops with expanded scales. The temperature dependence of magnetization is shown in the left inset. An in-plane external magnetic field of 10 kOe was applied. The diamagnetic contribution of the GaAs substrate has been subtracted.

exist three possible c axis alignments because of the three-fold symmetry of the substrate surface, similar to sample 1.

In the type-B islands, only the (0001)-oriented component is exclusively found. Moreover, flat (0001)-oriented MnAs films seem to fill the whole surface surrounding the type-A islands. In the black area in Fig. 7(b), only the Kikuchi pattern originating from the GaAs substrate was detected. The EBSD measurement fails to detect a surface layer if its thickness is smaller than 10–20 nm. Even in this area, islands formed by thin films are visible. The steps that run across these thin films are a few nm in height according to AFM measurements. (In Sec. IV, we will confirm by a resistance measurement that the coverage of the thin film is, at least, beyond the percolation threshold.)

To be precise, the crystal orientation in individual grains of the type-A islands determined by the EBSD measurements is not rigidly fixed to $(1\bar{1}0l)$ or (0001). The large fluctuations around the nominal orientations are also demonstrated using XRD measurements. When the sample was tilted and rotated around its surface normal while the detector was fixed at the exact Bragg conditions, i.e., in the so-called pole figure, the $(1\bar{1}01)$ reflection was found to be broader than the (0002) reflection (not shown). The fluctuations were roughly isotropic around the nominal orientations. The $(1\bar{1}01)$ reflection originates from the type-A islands, and so the peak is broad. On the contrary, the thin flat films of the type-B islands predominantly contribute to the (0002) reflection, providing the narrowness of the peak. For the reciprocal space map plotted in Fig. 8, the spread of the $(1\bar{1}01)$-reflection peak in ω is about twice as large as that of the (0002)-reflection peak. Individual domains in sample 3 that one would perceive from Figs. 7(b) and 7(c) actually consist of a number of grains that correspond to specific orientations associated with the fluctuations. Nevertheless, the grain size in sample 3 is about an order of magnitude larger than that in samples 1 and 2, presumably due to the long diffusion at the high substrate temperature.

Ordinary MnAs layers grown on GaAs(111)B are (0001)-oriented as the match in the in-plane rotation symmetry reduces the number of dangling bonds at the heterointerface.[6] The thin films (the type-B islands) sur-

rounding the type-A islands are also of this ordinary epitaxial orientation. In contrast, the thick islands (the type-A islands) are predominantly $(1\bar{1}0l)$-oriented. This suggests the importance of strain energy in the formation of the thick islands.[3,4] The type-A islands might have switched the crystal orientation to $(1\bar{1}0l)$ during the growth to take advantage of the small strain energy. Considering the rather insignificant role of the bonding energy manifested in SPE, the large thermal energy at the extremely high growth temperature may permit the switching. The other possible mechanism for the formation of the type-A islands is that the extraordinarily inhomogeneous growth may be an indication that the $(1\bar{1}0l)$ surfaces grow faster than the (0001) surface, which could happen, for instance, if the thermal decomposition of the $(1\bar{1}0l)$ surfaces at 600 °C is slower than that of the (0001) surface.

Kubo *et al.*[12] reported that a MnAs layer grown on GaAs(111)B at the temperature of 600 °C was of zinc-blende structure. Zinc-blende MnAs is attractive as it is theoretically predicted to be a half metal.[13] However, both XRD and EBSD measurements of our sample show no evidence for the presence of zinc-blende MnAs. The growth in Ref. 12 was performed at a growth rate of 210 nm/h, which is one order of magnitude larger than that for sample 3. The absence of zinc-blende MnAs in our sample might be related to the differences in the growth conditions.

IV. MAGNETIC AND ELECTRICAL PROPERTIES

In Fig. 9, we show the magnetization curves of sample 3 measured using a superconducting quantum interference device magnetometer at a temperature of 2 K. An in-plane external magnetic field was applied along the $[1\bar{1}0]$ and $[11\bar{2}]$ directions of the substrate for the solid and dotted curves, respectively. The coercive field (≈ 0.15 kOe) is similar to that in (0001)-oriented MnAs layers on GaAs(111)B grown at conventional growth temperatures.[14] In sample 1, the coercive and saturation fields when an external magnetic field was applied in the $[11\bar{2}]$ direction of the substrate were, re-
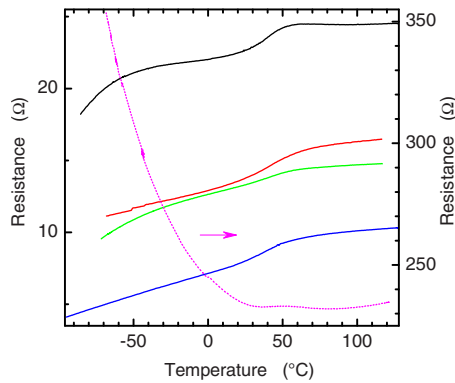
FIG. 10. (Color online) Temperature dependence of resistance in sample 3. Voltage probes with a separation of 4 μm were attached to single thick (type-A) islands for the solid curves. The distance between the voltage probes was 65 μm for the dotted curve.

FIG. 11. (Color online) Distribution of domain size [the probability density $p(s)$ vs domain size s] in quasi-one-dimensional square lattices. The number of square cells in the transverse direction of the chains is $N=1$, 2, and 4 for the triangles, circles, and squares, respectively. The degree of freedom f is 2 in (a) and (b) and 3 in (c) and (d).

spectively, 1 kOe and 25 kOe, see Ref. 3. That is, there are fewer pinning centers of domain walls at the reversal of magnetization in sample 3 than in sample 1. These comparisons indicate that the high growth temperature does not give rise to any degradation in terms of the magnetic properties. The smearing of the magnetization flip in the hysteresis loop can be ascribed to the misalignment between the external field and the easy axis orientation for some of the MnAs grains. We note that even out-of-plane components of magnetization may be generated for the type-A islands as the thickness is occasionally comparable to the width.

The temperature dependence of magnetization is shown in the left inset of Fig. 9. In bulk MnAs, magnetization disappears discontinuously at T_C due to a first-order phase transition. The phase transition in epitaxial MnAs layers on GaAs takes place, in contrast, over a finite temperature range due to the coexistence of ferromagnetic α phase and paramagnetic β phase, which originates from the strain imposed by the substrate.[15] The disappearance of magnetization consequently becomes continuous as the temperature dependence around T_C is governed by the approximately-linear variation of the phase fractions. The thermal expansion of MnAs is remarkably large (one order of magnitude larger than that of GaAs), and so the effects of the thermal strain are anticipated to be drastically enhanced in sample 3.[16] The high growth temperature is expected, for instance, to raise T_C as the tensile strain due to the thermal expansion mismatch will stabilize the ferromagnetic phase.[15] In sample 3, however, almost no change in T_C is found in comparison to bulk MnAs and MnAs layers grown at conventional temperatures. In addition, the phase transition occurs over a narrow temperature interval. For the type-A islands that will provide the dominant contribution to the magnetization (due to the probable large volume fraction), the strain imposed by the substrate is thus suggested to be insignificant because of their geometry.

In Fig. 10, we show the temperature dependence of resistance in sample 3. Here, the voltage probes with a separation of 4 μm were attached to individual type-A islands for the solid curves. Because of the inhomogeneity in the MnAs layer, the measurements were carried out at various locations in the layer. As the probe separation is larger than
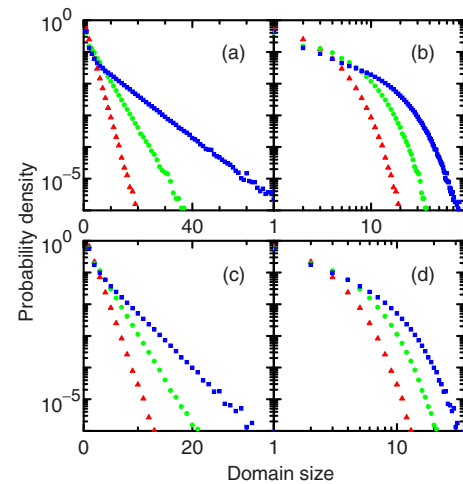
the grain size, a number of structural domains contribute to the resistance. Nevertheless, as manifested by the variety of the behavior of the curves, the ensemble averaging is less than the extent that the resistance exhibits a position-independent common characteristic.

The resistance change around 40 °C is associated with the phase transition at T_C. The temperature interval for the phase transition is only about 20 °C, in agreement with the interval in the magnetization measurement. In single-crystal MnAs layers on GaAs(001), the ratio of the resistances of the α and β phases at T_C was 0.7.[17] The small change in the resistance in Fig. 10 indicates that the resistance is dominated by the scattering from the domain boundaries[15] rather than the material properties of the two phases. The negative temperature coefficient for the β phase[17] is found only for the top-most curve. The mechanism that is responsible for the peculiar negative temperature coefficient is suggested to be sensitive to disorder.

For the dotted curve, the distance between the voltage probes is 65 μm, i.e., much larger than the size of the type-A islands. The resistance increases with decreasing temperature, in contrast to the metallic behavior in the type-A islands. The semiconducting behavior indicates that the layers that fill the space between the type-A islands are locally either extremely thin or composed of (Ga,Mn)As alloys.[18]

V. CONCLUSIONS

We have investigated the distribution of structural domains in MnAs layers on GaAs substrates using the EBSD technique. In the layers prepared on GaAs(111)B and GaAs(113)A by means of SPE, three types of ($1\bar{1}00$)-oriented domains and two types of ($21\bar{3}1$)-oriented domains coexist, respectively. The difference in the degree of freedom, together with the surface faceting, has been demonstrated to give rise to contrasting correlations between the surface morphology and the structural domains. In a MnAs layer grown at an extremely high temperature of 600 °C on

GaAs(111)B by conventional MBE, thick elongated islands consisting of $(1\bar{1}0l)$- and (0001)-oriented grains have been identified to be formed in the sea of (0001)-oriented thin flat films. The magnetic properties of the layer have been found to be altered only insignificantly by the high growth temperature, whereas clear degradations in the electrical properties have been observed. The different responses to the high growth temperature are attributed to the facts that the scattering from the domain boundaries plays an important role in the electrical properties and that the resistance is dominated by the thin parts of the layer although they are unimportant for magnetization due to their small volume fraction.

ACKNOWLEDGMENTS

APPENDIX: QUASI-ONE-DIMENSIONAL LATTICES

For one-dimensional chains, the distribution of the domain size is given by

$$p_1(s) = (f-1)f^{-s}, \tag{A1}$$

which corresponds to $\gamma = 0$ and $c = \ln f$ in terms of Eq. (1). As shown in the inset of Fig. 3(b), c in the two-dimensional lattices is rather proportional to f than to $\ln f$, at least, for small f.

A power-law behavior for small domain sizes emerges as soon as the number of square cells N in the transverse direction of the chain is larger than 1. For small values of N and s, direct calculation of the probability density $p_N(s)$ is easy. For instance, we find that the ratio $p_N(1):p_N(2):p_N(3):p_N(4)$ is given as

$$1:\frac{3(f-1)}{2f^2}:\frac{(f-1)(3f-1)}{f^4}:\frac{(f-1)(11f^2-8f+2)}{2f^6}, \tag{A2}$$

for $N=2$ and

$$1:\frac{(f-1)(5f-3)}{3f^3}:\frac{(f-1)^2(4f^2-2f+1)}{f^6}:\frac{(f-1)^2(29f^4-36f^3+26f^2-12f+3)}{3f^9}, \tag{A3}$$

for $N=3$. These relations already exhibit the trend of a power-law dependence.

In Fig. 11, we show the numerically determined variation of $p_N(s)$ when N is increased. The regime of the power-law distribution widens with increasing N. The following interpretation thus emerges for the power-law distribution with an exponential cut-off: The power-law contribution originates from the expansion of the islands in the transverse direction of the chains, and so the region of the power-law distribution spans for s up to $\sim N$. For $s > N$, $p_N(s)$ is determined mainly by the probability of elongating the islands in the direction of the chain, which will decay exponentially, as in the one-dimensional chains. The spread of the power-law regime for large N ceases when N becomes larger than the typical width of the islands. The distribution for two-dimensional lattices is hence given by a power law with an exponential cut-off rather than a pure power law. This is consistent with the characteristics in Figs. 2 and 3 that the exponential decay is more dominant for larger f as the islands shrink the size.

The power-law dependence is not fully developed for small N, and so fitting Eq. (1) to the data in Fig. 11 involves large error margins. (The uncertainty arises from the fact that $p_N(1)$ is usually larger than the value expected from extrapolating the behavior for $s \geq 2$.) Nevertheless, we have found that γ increases with N as $\gamma \sim 0.2(N-1)$ for the range $1 \leq N \leq 5$ that we numerically calculated. The dependence is roughly the same for $f=2$ and 3.

[1] V. H. Etgens, M. Eddrief, D. Demaille, Y. L. Zheng, and A. Ouerghi, J. Cryst. Growth **240**, 64 (2002).

[2] D. K. Satapathy, B. Jenichen, W. Braun, V. M. Kaganer, L. Däweritz, and K. H. Ploog, J. Phys. D **38**, A164 (2005).

[3] Y. Takagaki, C. Herrmann, B. Jenichen, J. Herfort, and O. Brandt, Appl. Phys. Lett. **92**, 101918 (2008); **92**, 179901(E) (2008).

[4] Y. Takagaki, C. Herrmann, B. Jenichen, and O. Brandt, Phys. Rev. B **78**, 064115 (2008).

[5] Y. Takagaki, B. Jenichen, C. Herrmann, and J. Herfort, Phys. Rev. B **80**, 014116 (2009).

[6] L. Däweritz, Rep. Prog. Phys. **69**, 2581 (2006).

[7] J. H. Song, Y. Cui, J. J. Lee, S. L. Cho, and J. B. Ketterson, J. Appl. Phys. **103**, 07B501 (2008).

[8] J. W. Essam, J. Phys. A **22**, 4927 (1989).

[9] R. Hilfer and P. Meakin, Z. Phys. B **88**, 223 (1992); T. Vicsek and F. Family, Phys. Rev. Lett. **52**, 1669 (1984).

[10] M. Kolb, Phys. Rev. Lett. **53**, 1653 (1984).

[11] F. Xu, P. W. Huang, J. H. Huang, W. N. Lee, T. S. Chin, H. C. Ku, and Y. W. Du, J. Appl. Phys. **107**, 063909 (2010).

[12] K. Kubo, Y. Kato, K. Kanai, J. Ohta, H. Fujioka, and M. Oshima, J. Cryst. Growth **310**, 4535 (2008).

[13] S. Sanvito and N. A. Hill, Phys. Rev. B **62**, 15553 (2000); I. Galanakis and P. Mavropoulos, *ibid.* **67**, 104417 (2003); J. E. Pask, L. H. Yang, C. Y. Fong, W. E. Pickett, and S. Dag, *ibid.* **67**, 224420 (2003).

[14] L. Däweritz, C. Herrmann, J. Mohanty, T. Hesjedal, K. H. Ploog, E. Bauer, and A. Locatelli, J. Vac. Sci. Technol. B **23**, 1759 (2005).

[15] Y. Takagaki, C. Herrmann, J. Herfort, C. Hucho, and K.-J. Friedland, Phys. Rev. B **78**, 235207 (2008).

[16] V. Garcia, Y. Sidis, M. Marangolo, F. Vidal, M. Eddrief, P. Bourges, F. Maccherozzi, G. Panaccione, and V. H. Etgens, Phys. Rev. Lett. **99**, 117205 (2007).

[17] Y. Takagaki, L. Däweritz, and K. H. Ploog, Phys. Rev. B **75**, 035213 (2007).

[18] Y. Osafune, G. S. Song, J. I. Hwang, Y. Ishida, M. Kobayashi, K. Ebata, Y. Ooki, A. Fujimori, J. Okabayashi, K. Kanai, K. Kubo, and M. Oshima, J. Appl. Phys. **103**, 103717 (2008).